Asymmetric Separated Flows at Supersonic Speeds

M. J. Siclari*
Grumman Corporate Research Center, Bethpage, New York 11714

An efficient multigrid, central difference, finite volume Navier-Stokes solver is used to study the "natural occurrence" of steady, anomalous, asymmetric separated "locally conical" flow solutions at high incidence and at supersonic speeds. The study documents the regime in which asymmetric conical flows are likely to occur as a function of Mach number and cone angle. It is also shown that the existence of asymmetric flows is not unique to circular cones and is exhibited for a variety of cross-sectional shapes. The elimination of asymmetric flow behavior with the addition of strakes is also demonstrated. This paper also presents a parabolized Navier-Stokes solution for a three-dimensional ogive cylinder body exhibiting asymmetric flow behavior.

Introduction

ON slender-nosed aircraft flying at zero sideslip and at a high angle of attack where the incidence exceeds twice the nose angle, the flow (which at lower incidence was symmetric) can become very asymmetric due to the generation of asymmetric vortices. This phenomenon has been observed both experimentally and in flight for several decades. The sudden onset of the sideforce may result in lateral instability. The cause of this anomalous asymmetry in the flow has been debated since it was first discovered.

One of the first indications that this phenomenon was not due to asymmetric imperfections in geometry or wind tunnel characteristics came from the work of Fiddes.[1] Fiddes demonstrated small disturbance, incompressible flow computations for cones with vortex sheets modeled by vortex filaments that exhibited asymmetric vortex patterns. Later, Marconi[2] carried out supersonic Euler computations in conjunction with a flow separation model that also exhibited asymmetric vortex patterns for circular cones in the same incidence regime as Fiddes. Both of these studies indicated the possible existence of multiple solutions or bifurcated asymmetric solutions. Unlike Fiddes, Marconi found that the Euler symmetric solution proved to be unstable.

More recently, Siclari and Marconi[3] were able to obtain "locally conical" steady laminar Navier-Stokes full-plane solutions for a 5-deg cone at a supersonic Mach number of 1.8 that exhibited a continuous range of naturally occurring bifurcated solutions without the imposition of a viscous separation model, geometric perturbation, or asymmetric boundary condition. Unlike other studies (e.g., Ref. 4), it was found in Ref. 3 that the asymmetric conical viscous solutions could be achieved naturally without any geometric irregularities or other perturbations to trigger them. This naturally occurring phenomenon may be distinct or act in conjunction with another phenomenon, such as seen by other investigators such as Degani and Schiff,[4,5] where small geometric or other flow perturbations at the apex may trigger or be amplified into a more global asymmetric flow behavior.

When started from symmetric initial conditions, the conical solutions presented in Ref. 3 would be driven to the symmetric solution until the residuals approached the truncation error of the machine. At this point, the residual would rise almost to its original level and then diminish again and finally converge to machine zero, and the solution would lock onto one of the two mirror image asymmetric solutions. It was also discovered that the solution could be driven directly to the asymmetric solution by specifying asymmetric initial conditions. The solutions presented in Ref. 3 indicated the sudden onset of bifurcated asymmetric solutions at a critical ratio of incidence to cone half-angle of somewhat greater than two. It was also discovered that with increasing incidence the sideforce peaked, and then the bifurcated asymmetric solutions rapidly returned to a single symmetric one with further increase in incidence. The predicted sideforce based on these "locally conical" solutions compared remarkably well to experimental data as shown in Fig. 1 (from Ref. 3). To eliminate doubts about the numerical solutions, the computations were all carried out to machine zero. During the course of this study, it was also observed that the symmetric solution for the circular cone was, in fact, unstable in agreement with the findings of Marconi in Ref. 2. These asymmetric locally conical solutions have been corroborated by Kandil et al.[6] using other codes such as CFL3D.[7]

The present study extends the work of Ref. 3 to include a variety of cone angles, Mach numbers, and cross-sectional shapes in an attempt to document the domain of occurrence of asymmetric solutions based on the locally conical Navier-Stokes equations. All the solutions were computed at a Reynolds number per unit length of 100,000 with the assumption of laminar flow and adiabatic wall conditions. The paper also presents a parabolized Navier-Stokes solution over a three-dimensional body shape using the conical solution as initial data.

Computational Procedure

The computational procedure[8,9] used in the present study is briefly outlined in this section. The unsteady Navier-Stokes equations in conservation form and Cartesian coordinates can be written as

$$\frac{\partial \boldsymbol{Q}}{\partial t} + \frac{\partial(\boldsymbol{F} - \boldsymbol{F}_v)}{\partial x} + \frac{\partial(\boldsymbol{G} - \boldsymbol{G}_v)}{\partial y} + \frac{\partial(\boldsymbol{H} - \boldsymbol{H}_v)}{\partial z} = 0 \quad (1)$$

where the flux vectors $\boldsymbol{F}$, $\boldsymbol{G}$, and $\boldsymbol{H}$ are the inviscid terms and $\boldsymbol{F}_v$, $\boldsymbol{G}_v$, and $\boldsymbol{H}_v$ represent the viscous shear stress and heat flux terms. The conservation variables and flux vectors are defined as follows:

$$\boldsymbol{Q} = \begin{bmatrix} \rho \\ \rho u \\ \rho v \\ \rho w \\ e \end{bmatrix} \qquad \boldsymbol{F} = \begin{bmatrix} \rho u \\ \rho u^2 + p \\ \rho uv \\ \rho uw \\ \rho uh \end{bmatrix}$$

Presented as Paper 90-0595 at the AIAA 28th Aerospace Sciences Meeting, Reno, NV, Jan. 8–11, 1990; received Feb. 27, 1990; revision received May 30, 1991; accepted for publication June 10, 1991.

*Senior Staff Scientist. Associate Fellow AIAA.

$$\boldsymbol{G} = \begin{bmatrix} \rho v \\ \rho vu \\ \rho v^2 + p \\ \rho vw \\ \rho vh \end{bmatrix} \quad \boldsymbol{H} = \begin{bmatrix} \rho w \\ \rho wu \\ \rho wv \\ \rho w^2 + p \\ \rho wh \end{bmatrix}$$

$$\boldsymbol{F}_v = \begin{bmatrix} 0 \\ \tau_{ss} \\ \tau_{xy} \\ \tau_{xz} \\ F_h \end{bmatrix} \quad \boldsymbol{G}_v = \begin{bmatrix} 0 \\ \tau_{xy} \\ \tau_{yy} \\ \tau_{yz} \\ G_h \end{bmatrix} \quad \boldsymbol{H}_v = \begin{bmatrix} 0 \\ \tau_{xz} \\ \tau_{yz} \\ \tau_{zz} \\ H_h \end{bmatrix}$$

where u, v, and w are the Cartesian velocity components in the x, y, and z directions, respectively; ρ is the density; p the pressure; and e the total energy. The pressure and total enthalpy are related to the flow variables by

$$e = \frac{p}{\gamma - 1} + \frac{1}{2}\rho(u^2 + v^2 + w^2)$$

$$h = \frac{e + p}{\rho} \tag{2}$$

where γ is the ratio of specific heats.

The Cartesian equations can be transformed to a spherical or conical coordinate system by the following transformation:

$$\bar{x} = x/z, \; \bar{y} = y/z, \; R^2 = x^2 + y^2 + z^2 \tag{3}$$

If all lengths are scaled by L, density and velocities by the freestream density (ρ_∞) and speed of sound (a_∞), energy and pressure by ($\rho_\infty a_\infty^2$), and time by (L/a_∞), the dimensionless Navier-Stokes equations can be rewritten in spherical or conical coordinates as

$$\frac{\partial \boldsymbol{Q}}{\partial t} + \frac{\Omega}{R}\left[\frac{\partial}{\partial \bar{x}}\left(\bar{\boldsymbol{F}} - \frac{1}{R_e}\bar{\boldsymbol{F}}_v\right) + \frac{\partial}{\partial \bar{y}}\left(\bar{\boldsymbol{G}} - \frac{1}{R_e}\bar{\boldsymbol{G}}_v\right) + 2\left(\bar{\boldsymbol{I}} - \frac{1}{R_e}\bar{\boldsymbol{I}}_v\right)\right] + \frac{1}{\Omega}\frac{\partial}{\partial R}\left(\bar{\boldsymbol{H}} - \frac{1}{R_e}\bar{\boldsymbol{H}}_v\right) = 0 \tag{4}$$

where the flux vectors ($\bar{\boldsymbol{F}}$, $\bar{\boldsymbol{G}}$, $\bar{\boldsymbol{H}}$, $\bar{\boldsymbol{I}}$) and ($\bar{\boldsymbol{F}}_v$, $\bar{\boldsymbol{G}}_v$, $\bar{\boldsymbol{H}}_v$, $\bar{\boldsymbol{I}}_v$) are defined as

$$\bar{\boldsymbol{F}} = \begin{bmatrix} \rho\bar{U} \\ \rho u\bar{U} + p \\ \rho v\bar{U} \\ \rho w\bar{U} - \bar{x}p \\ \rho h\bar{U} \end{bmatrix} \quad \bar{\boldsymbol{G}} = \begin{bmatrix} \rho\bar{V} \\ \rho u\bar{V} \\ \rho v\bar{V} + p \\ \rho w\bar{V} - \bar{y}p \\ \rho h\bar{V} \end{bmatrix}$$

$$\bar{\boldsymbol{H}} = \begin{bmatrix} \rho\bar{W} \\ \rho u\bar{W} + \bar{x}p \\ \rho v\bar{W} + \bar{y}p \\ \rho w\bar{W} - p \\ \rho h\bar{W} \end{bmatrix} \quad \bar{\boldsymbol{I}} = \begin{bmatrix} \rho w \\ \rho uw \\ \rho vw \\ \rho w^2 + p \\ \rho hw \end{bmatrix}$$

$$\bar{\boldsymbol{F}}_v = \begin{bmatrix} 0 \\ \tau_{xx} - \bar{x}\tau_{xz} \\ \tau_{xy} - \bar{x}\tau_{yz} \\ \tau_{xz} - \bar{x}\tau_{zz} \\ F_h - \bar{x}H_h \end{bmatrix} \quad \bar{\boldsymbol{G}}_v = \begin{bmatrix} 0 \\ \tau_{xy} - \bar{y}\tau_{xz} \\ \tau_{yy} - \bar{y}\tau_{yz} \\ \tau_{yz} - \bar{y}\tau_{zz} \\ G_h - \bar{y}H_h \end{bmatrix}$$

$$\bar{\boldsymbol{H}}_v = \begin{bmatrix} 0 \\ \bar{x}\tau_{xx} + \bar{y}\tau_{xy} + \tau_{xz} \\ \bar{x}\tau_{xy} + \bar{y}\tau_{yy} + \tau_{yz} \\ \bar{x}\tau_{xz} + \bar{y}\tau_{yz} + \tau_{zz} \\ \bar{x}F_h + \bar{y}G_h + H_h \end{bmatrix} \quad \bar{\boldsymbol{I}}_v = \begin{bmatrix} 0 \\ \tau_{xz} \\ \tau_{yz} \\ \tau_{zz} \\ H_h \end{bmatrix}$$

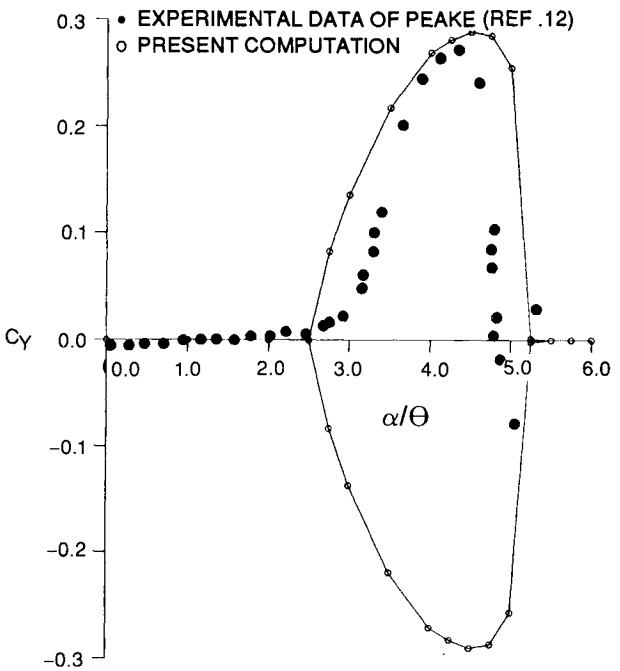

Fig. 1 Computed sideforce coefficients and surface pressures for the 5-deg cone at $M_\infty = 1.80$, $R_e = 1 \times 10^5$ (from Ref. 3).

and

$$\bar{U} = u - \bar{x}w$$

$$\bar{V} = v - \bar{y}w$$

$$\bar{W} = u\bar{x} + v\bar{y} + w$$

$$\Omega = (1 + \bar{x}^2 + \bar{y}^2)^{1/2}$$

$$(R_e)^{-1} = M_\infty/R_{e\infty}$$

Assuming Stokes' hypothesis, the shear stress and heat flux terms become

$$\tau_{xx} = 2\bar{\mu}u_x - \sigma \qquad \tau_{xy} = \bar{\mu}(u_y + v_x)$$

$$\tau_{yy} = 2\bar{\mu}u_y - \sigma \qquad \tau_{xz} = \bar{\mu}(u_z + w_x)$$

$$\tau_{zz} = 2\bar{\mu}u_z - \sigma \qquad \tau_{yz} = \bar{\mu}(v_z + w_y)$$

$$F_h = u\tau_{xx} + v\tau_{xy} + w\tau_{xz} + A\bar{\mu}\,a_x^2$$

$$G_h = u\tau_{xy} + v\tau_{yy} + w\tau_{yz} + A\bar{\mu}\,a_y^2$$

$$H_h = u\tau_{xz} + v\tau_{yz} + w\tau_{zz} + A\bar{\mu}\,a_z^2$$

where

$$\sigma = \tfrac{2}{3}\bar{\mu}(u_x + v_y + w_z), \; A = [P_r(\gamma - 1)]^{-1}$$

and Sutherland's law has been assumed for the viscosity,

$$\bar{\mu} = a^3\left[\frac{1 + S}{a^2 + S}\right]$$

and S is a constant.

Equation (4) can be written in integral form as

$$\frac{\partial}{\partial t}\iint_s \boldsymbol{Q}\,d\bar{x}\,d\bar{y} + \oint(\hat{\boldsymbol{F}}\,d\bar{y} - \hat{\boldsymbol{G}}\,d\bar{x}) + 2\iint \hat{\boldsymbol{I}}\,d\bar{x}\,d\bar{y} + \frac{R}{\Omega^2}\iint \frac{\partial \hat{\boldsymbol{H}}}{\partial R}\,d\bar{x}\,d\bar{y} = 0 \tag{5}$$

where

$$\hat{F} = \bar{F} - \frac{1}{R_e}\bar{F}_v$$

$$\hat{G} = \bar{G} - \frac{1}{R_e}\bar{G}_v$$

$$\hat{I} = \bar{I} - \frac{1}{R_e}\bar{G}_v$$

$$\hat{t} = \frac{\Omega}{R}t$$

$$\hat{H} = \bar{H}$$

The coordinate coefficient metric Ω/R has been absorbed into the unsteady term since only steady-state solutions are sought. For locally conical flows, the $\partial\hat{H}/\partial R$ is assumed to be identically zero. Conicity does not truly exist for viscous flows since the viscous shear stresses retain a dependence on the spatial coordinate R even when the R derivatives are neglected. Hence, the flows computed are referred to as "locally conical" by choosing a fixed value for the R coordinate. In the solutions to follow, the local conical Navier-Stokes equations are solved on a unit sphere. Due to the dependence on R in the viscous terms, the boundary layer does not scale with R. It is well known that the boundary layer on a cone grows like the square root of R.

For three-dimensional marching computations, the Navier-Stokes equations are parabolized by neglecting the viscous terms in the R direction or by setting $\hat{H} = \bar{H}$. It should also be pointed out that the equations retain both viscous crossflow terms in contrast to the usual thin-layer approximation.

A node-centered finite volume scheme is applied to a discretized version of Eq. (5) in the crossflow plane. Both the flow variables Q and the residuals are stored at node points. The cell-centered fluxes are first computed over each cell of the grid by summing the fluxes across the four individual sides of the cell in a fashion similar to a cell-centered scheme. Unlike the cell-centered scheme, the flow variables are stored at the endpoints of each side constituting the boundaries of a cell. This has the potential of yielding a more accurate estimate for the flux across the sides of a highly skewed or irregular mesh than that provided by a cell-centered scheme. The residual at each node point is then computed by summing the cell-centered fluxes of the four cells surrounding that node point. In discretized form, the conical terms of Eq. (5) can be written at a node point i,j as

$$\Delta S\frac{\Delta Q}{\Delta\hat{t}} + \sum_{\text{cell}=1}^{4}\sum_{\text{side}=1}^{4}(\hat{F}\Delta\bar{y} - \hat{G}\Delta\bar{x}) + 2\hat{I}\Delta S + \frac{R}{\Omega^2}\hat{H}_R\Delta S = 0 \tag{6}$$

where $\hat{F}$ and $\hat{G}$ are the total side fluxes that include viscous terms evaluated at the node points. The area ΔS is defined as

$$\Delta S = \sum_{\text{cell}=1}^{4}\Delta A$$

and is the sum of the areas of the four individual cells surrounding a node point. Thus, the node residuals correspond to flux balances on interlaced control volumes, each consisting of a group of four cells.

To include the viscous shear stress and heat flux terms, the velocity derivatives are estimated at the node points using central difference formulas in a computational space. The mesh transformation derivatives needed for the velocity derivatives are computed numerically. At the boundary, one-sided differences are used to estimate the velocity derivatives.

A blend of second- and fourth-order differences is used for added artificial dissipation. The fourth-order differences are added as background dissipation to prevent odd and even point decoupling. The second-order differences are added primarily to smooth out oscillations in regions of severe pressure gradients associated with shock waves. A detailed account of the form of the dissipation can be found in Refs. 8–10.

The set of unsteady governing equations can be represented as

$$\frac{\partial Q}{\partial t} + \frac{1}{\Delta S}R_{\bar{x}\bar{y}}(Q) + \frac{1}{\Delta S}D_{\bar{x}\bar{y}}(Q) = 0 \tag{7}$$

where the operator $R_{\bar{x}\bar{y}}$ represents the spatial crossflow finite volume and radial finite difference approximation to the residual, and $D_{\bar{x}\bar{y}}$ represents the added artificial dissipation. A modified fourth-order Runge-Kutta scheme is used to integrate the set of ordinary differential equations defined by Eqs. (6) and (7) in the following manner:

$$Q^{(\ell)} = Q^{(0)} - \alpha_\ell\frac{\Delta t}{\Delta S}(R_{\bar{x}\bar{y}}^{(\ell-1)} + D_{\bar{x}\bar{y}}^{(0)}) \tag{8}$$

where

$$\alpha_\ell = \left(\frac{1}{4}, \frac{1}{3}, \frac{1}{2}, 1\right) \text{ for } \ell = 1,4$$

The Runge-Kutta scheme for three-dimensional marching computations is made implicit in the radial marching direction by including the R terms in each time step of the multistage integration scheme. This essentially removes any constraints on the marching step size and allows for very large spatial increments in the marching direction. The bracketed superscript refers to the stages of the Runge-Kutta scheme. The dissipative terms are frozen throughout the multistage integration scheme.

Local time stepping and implicit residual smoothing is utilized in the crossflow plane to accelerate convergence. The residual smoothing is applied to alternate stages, the second and the fourth stages of the Runge-Kutta scheme.

A multigrid method is used to accelerate the convergence of the basic multistage time-stepping scheme. The idea behind the multigrid scheme is to speed up the evolution process by using a series of coarser grids that introduce larger scales and larger time steps while requiring less costly computations. The present multigrid scheme follows the work of Jameson[10] and is presented in more detail in Ref. 8.

The present method has developed into a code called MIM3D (i.e., Multigrid Implicit Marching), which at the first step computes a local conical flow solution by neglecting the R derivatives. Three-dimensional solutions are then obtained using a hybrid implicit marching method which computes the crossflow terms by the same finite volume method used for locally conical flows and includes marching derivatives using a finite difference upwind approximation. Since the equations are formulated in a spherical coordinate system, the marching takes place on R = constant surfaces.

After presenting results for conical flows, the last section presents a three-dimensional result.

Discussion of Results

Convergence Histories

If asymmetric solutions exist for circular cones, one might expect them to exist for other types of cross sections. In fact, Fiddes[11] was able to find asymmetric solutions for elliptic cones using linear theory. Figure 2 shows some typical grids

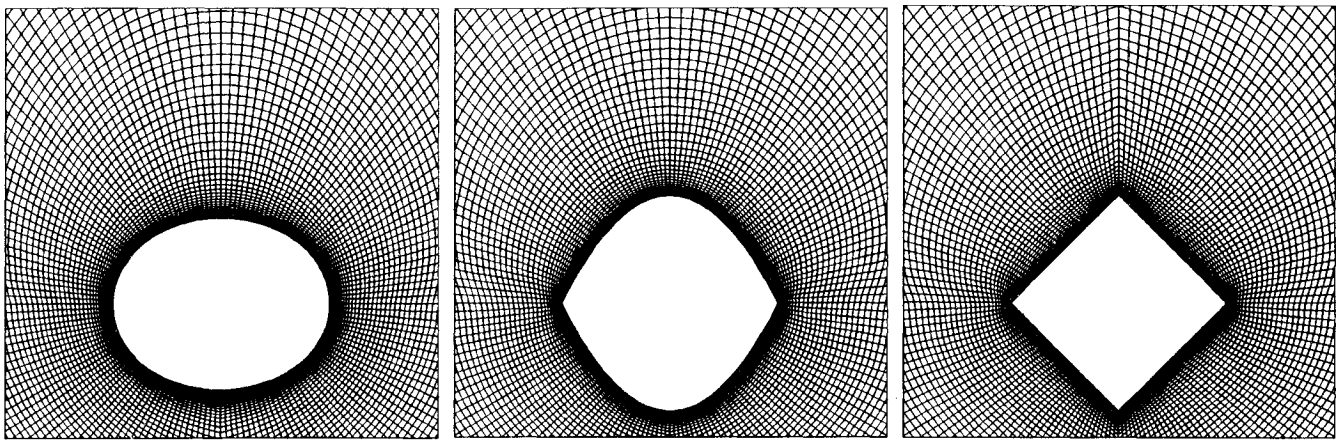

Fig. 2 Typical viscous grids (161 × 81) used for three different types of cross sections.

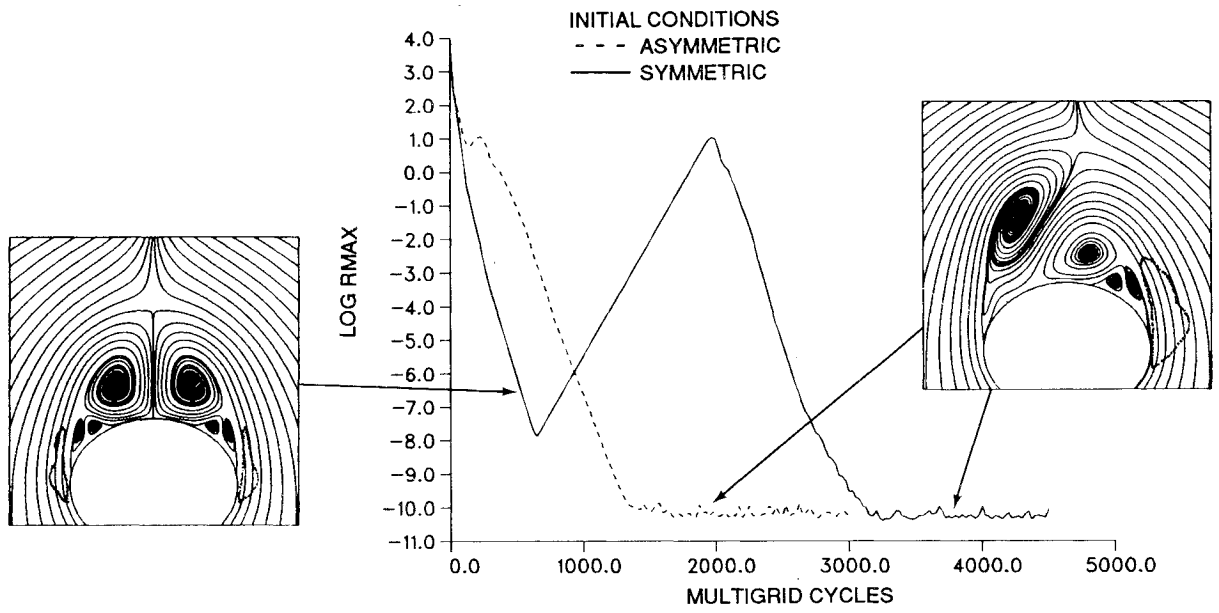

Fig. 3 Convergence behavior of an elliptic cone at $M_\infty = 1.80$ and $\alpha = 20$ deg.

used in this study for three different cross sections. Full-plane grids of 161 × 81 were used with the grid cut located on the windward symmetry plane. Figure 2a shows an elliptic cross section, Fig. 2b shows a biparabolic cross section, and Fig. 2c shows a biwedge cross section. As in Ref. 3, a viscous sublayer grid was patched into an existing Euler-type grid in order to resolve the boundary layer. All of the solutions in this section were computed at a constant Mach number of 1.8 and incidence of 20 deg with a semimajor axis half-angle of 5 deg.

Figure 3 shows the convergence behavior of a 5 deg by 4 deg elliptic cone. The solid line shows the convergence history in terms of maximum residual versus multigrid cycles for the computation started with symmetric initial freestream conditions. The solution converges by almost 12 orders of magnitude when suddenly the residual error begins to increase to almost its original level. Further iterations then show a decline in residual until finally the computation converges to machine zero and remains at that level for subsequent multigrid cycles. The solution was output at the first minimum in residual and at machine zero. As indicated by the crossflow streamline patterns inset on the figure, the first minimum in residual corresponds to a symmetric solution, and the machine zero residual corresponds to an asymmetric solution. The dashed lines superimposed on the streamline patterns correspond to crossflow sonic lines. Interior to these regions the crossflow Mach number is supersonic. This kind of behavior is identical to that discovered in Ref. 3 for circular cones and demonstrates the weak instability of the symmetric solution. The dashed line in Fig. 3 corresponds to the same computation that was started with slightly asymmetric freestream initial conditions, a sideslip of 3 deg. It should be mentioned that after the first iteration, all subsequent iterations were computed with symmetric outer boundary freestream conditions enforced. For this computation, the residual declines monotonically to machine zero but at a slightly lower rate than the computation started with symmetric initial conditions. The resulting solution started with asymmetric initial conditions is the same asymmetric solution achieved at machine zero with the symmetric start. An interesting aspect of Fig. 3 with a symmetric start is that the buildup of the error leading to an asymmetric solution occurs over as many multigrid cycles as it takes to achieve a machine zero result starting with asymmetric initial conditions.

Figure 4 shows the same type of plot for the biparabolic cross section with a major axis half-angle of 5 deg and an aspect ratio of 1. The solution for this type of cross section becomes more difficult to achieve, probably due to the sharp leading edge and the extreme metric variations occurring in this region. The case of a sharp leading edge is interesting.

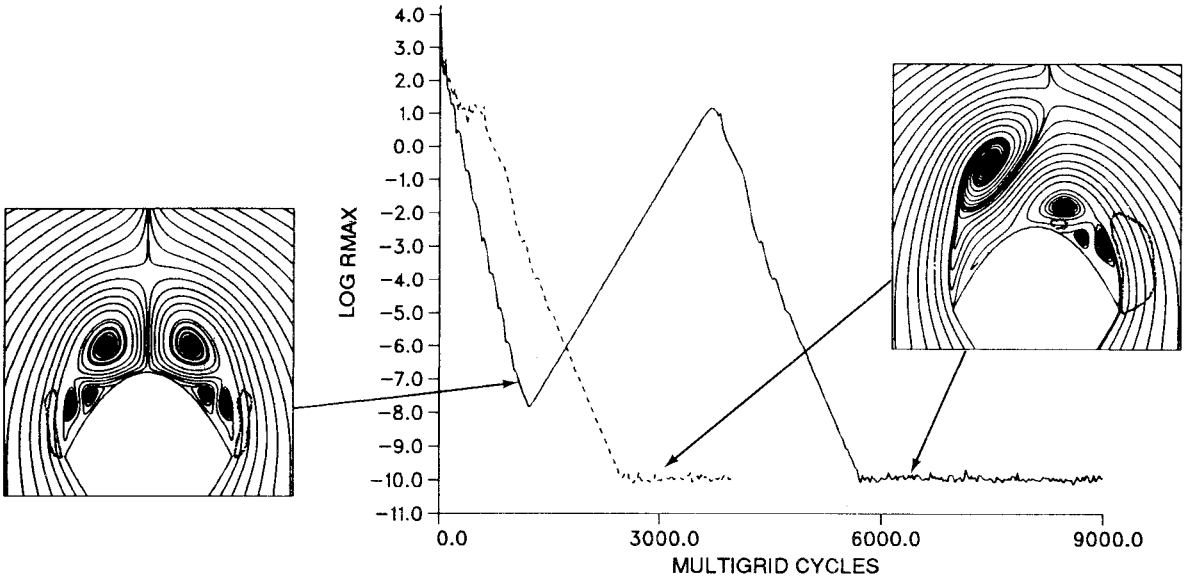

Fig. 4 Convergence behavior of a biparabolic cone at $M_\infty = 1.80$ and $\alpha = 20$ deg.

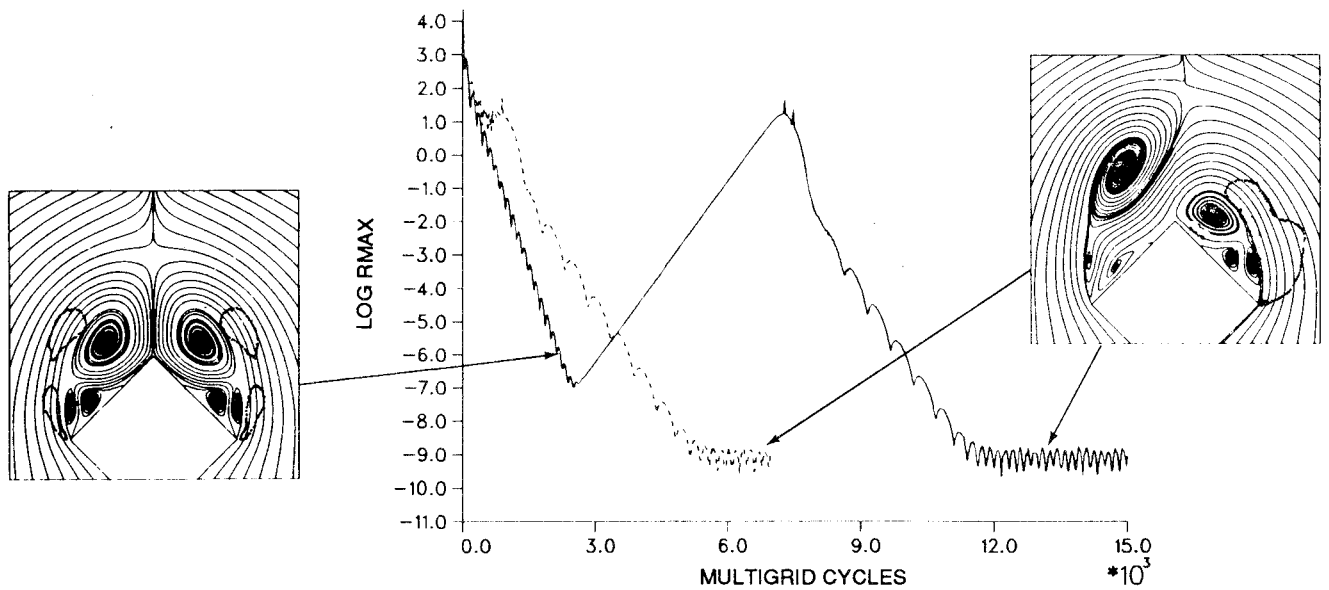

Fig. 5 Convergence behavior of a biwedge cone at $M_\infty = 1.80$ and $\alpha = 20$ deg.

One would think that asymmetric solutions would not exist because the flow is constrained to separate at the leading edges, if one assumes that the separation points play a large role in determining the asymmetric behavior. The identical behavior that was shown for the elliptic cone also occurs for this cross section, although it takes twice as many multigrid cycles to occur. Evidently, the asymmetric flow behavior is driven by the dynamic interaction of the vortices.

Figure 5 further shows a similar plot for a biwedge cross section with a 5-deg half-angle and an aspect ratio of unity. This solution is even more difficult to achieve, taking 12,000 multigrid cycles to achieve machine zero with a symmetric start. The behavior observed for the previous cross-sectional shapes persists in that an asymmetric solution exists with the symmetric solution unstable.

Figure 6 shows the surface pressure distributions for the three different cross sections at $M_\infty = 1.8$, $\alpha = 20$ deg. The sharp leading edges of the parabolic and wedge cross sections are indicated by the rapid expansions followed by an abrupt recompression.

To study the behavior of these flows, Figs. 3 to 5 show that it would be difficult and very computationally expensive to try to achieve asymmetric solutions using a symmetric start and at the same time converge to machine zero. Hence, all of the solutions to follow were generated with asymmetric initial freestream conditions and converged 9 orders of magnitude. Figures 3 to 5 have demonstrated that the symmetric solution only becomes unstable for noncircular cross sections after about 12 orders of magnitude.

Hence, asymmetric conical viscous solutions exist for a variety of other cross-sectional shapes and are not restricted exclusively to circular cones. The next section attempts to first define the regime of asymmetric flows for circular cones.

Conical Flows: Circular Cones

Using the same type of full-plane grids (161 × 81) used in Ref. 3, a matrix array of viscous locally conical flow solutions was generated for Mach numbers ranging from 1.4 to 3.0 and cone half-angles of 5, 6, 7, and 8 deg at 20-deg angle of attack. A sample of the results of this study is indicated by Fig. 7 with entropy contours. All of these solutions were generated using asymmetric initial freestream conditions and converged nine orders of magnitude. This was done only to conserve computer time. For the 5-deg cone (Fig. 7a), asymmetric solutions

were achieved up to a Mach number of 2.6. At Mach 3, only a symmetric solution could be achieved. Similar results were obtained for the 6-deg cone. The 7-deg cone returns to a symmetric solution very quickly as the Mach number increases to 2.2. Finally, the 8-deg cone shows only a minor asymmetry at Mach 1.4 and is clearly symmetric at Mach 1.8. Figure 7b shows the behavior of the solutions at $M_\infty = 1.4$ with increasing cone angles. Hence, the existence of these solutions is affected by both Mach number and cone angle. It is also clear that the asymmetric behavior declines very rapidly with increase in cone angle at 20-deg angle of attack. The asymmetric solutions shown represent only one root of the bifurcation. Mirror images of these solutions also exist. The significant feature of Fig. 7 is that the asymmetric/symmetric behavior of the solutions is continuous and the general trends with Mach number and cone angle are in agreement with experimental observations.[12]

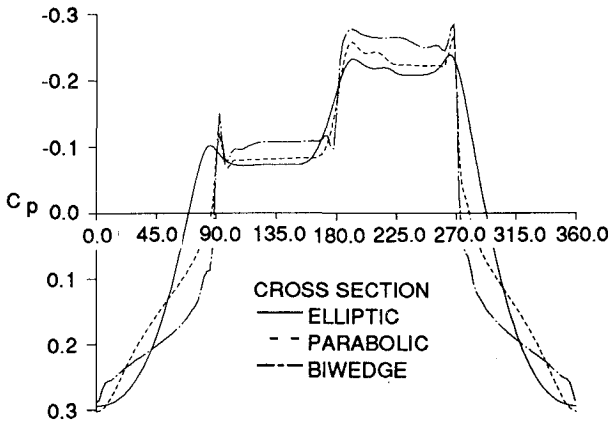

Fig. 6 Asymmetric surface pressure distributions for elliptic, biparabolic, and biwedge cross sections at $M_\infty = 1.80$ and $\alpha = 20$ deg.

Figure 8 shows the computed crossflow streamlines for the 5-deg cone as a function of increasing Mach number. At the lower Mach numbers, four vortices are present in the solution with the lower vortex lying near the symmetry plane. As the Mach number is increased, this vortex migrates to the right-hand side of the cone and a small fifth vortex emerges. At the symmetric solution, three vortices are present on each side. This behavior also occurs for the 6-deg cone. It is also apparent that the return to a symmetric solution coincides with the development of supersonic crossflow regions on both sides of the cone. The supersonic crossflow regions are indicated by dotted lines on the figures. In all cases, as the solution becomes symmetric, supersonic crossflow regions first appear on one side and then on both. Evidently, the appearance of supersonic crossflow diminishes communication between the opposing separated flows, and it may be that the interaction of these separated flows plays a large role in causing the asymmetric behavior.

Mach numbers below 1.4 were not investigated because of eventual shock detachment which precludes conical flow behavior. Figure 9 summarizes the results obtained in this study for supersonic circular cone solutions showing the regime in which asymmetric solutions can be found with respect to Mach number and cone angle at a fixed incidence of 20 deg.

Straked Cone

Aircraft designers have known for some time that if asymmetric flow occurs at high incidence, leading to lateral instability due to sideforces, this situation can be alleviated by fitting the nose with a small strake. The strake tends to eliminate the occurrence of asymmetric behavior. Figure 10a shows the crossflow streamline pattern computed for a 5-deg cone

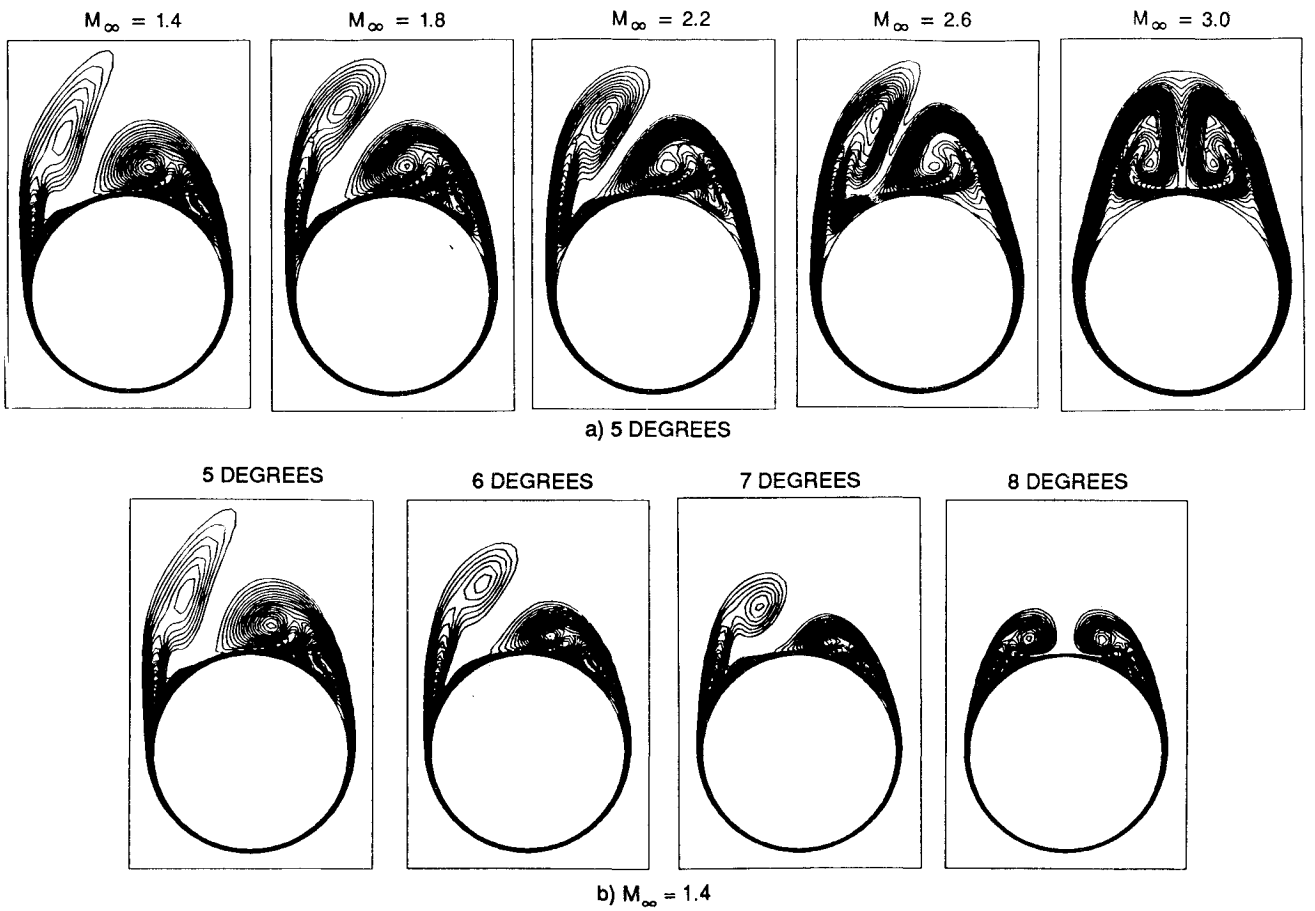

Fig. 7 Entropy contours computed for 5-, 6-, 7-, and 8-deg half-angle circular cones at Mach numbers from 1.4 to 3.0 and $\alpha = 20$ deg.

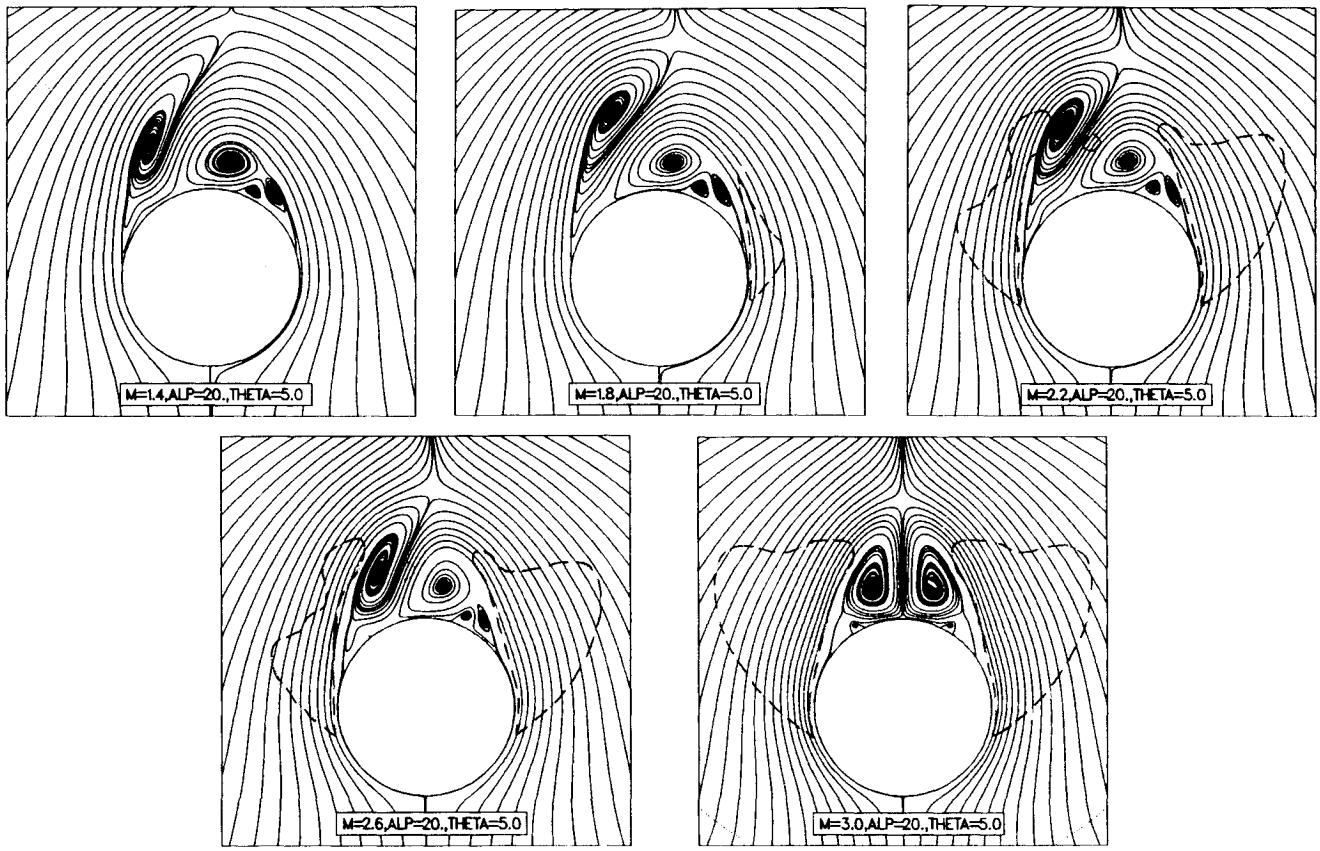

Fig. 8 Crossflow streamline patterns computed for a 5-deg circular cone at α = 20 deg and Mach numbers from 1.4 to 3.0.

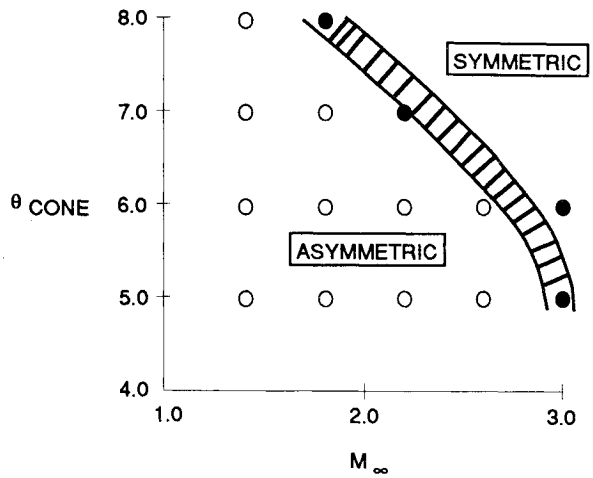

Fig. 9 Regime of supersonic conical asymmetric flows for circular cones at α = 20 deg.

at M = 1.8 and α = 20 deg. Figure 10b shows the same cone fitted with a 7-deg biwedge strake. The computation was started the same way as the one in Fig. 10a, with slightly asymmetric initial freestream conditions to bring out any asymmetric solutions that might exist. The presence of a small strake has a dramatic effect on the flowfield. The straked cone solution is symmetric as expected. In addition, a complex pattern of vortices evolve with the addition of a small strake. All other local conical solutions up to now had at the most six vortices. The pattern shown in Fig. 10b shows a symmetric set of five vortices or a total of 10 vortices. The windward cone strake juncture shows a small vortex and separation due to the adverse pressure gradient generated by the windward surface of the strake. A large reverse flow separation and vortex occurs on the leeward surface. The two largest vortices are connected by a crossflow stagnation saddle point. Hence, the computation verifies that the addition of a small strake eliminates the asymmetric behavior.

Conical Flows: Arbitrary Cross Sections

Figure 11 summarizes the effects of aspect ratio on three cross-sectional shapes: elliptic, biparabolic, and biwedge. Figure 11 shows entropy contours for the three types of cross section with decreasing aspect ratio at a constant Mach number of 1.8, incidence of 20 deg, and a major axis half-angle of 5 deg. In Fig. 11a, the elliptic cone exhibits asymmetric behavior until an aspect ratio of 0.5. The asymmetric behavior has vanished at an aspect ratio of 0.4. Fiddes computed a similar behavior with linear theory and found that the asymmetry vanished at a 0.52 aspect ratio. The viscous solutions indicate a slightly more persistent asymmetric behavior. Figure 11b shows the behavior for the biparabolic cross section. For this cross section, the asymmetric behavior disappears more abruptly and becomes symmetric by an aspect ratio of 0.5. In Fig. 11c, the asymmetric behavior vanishes even faster with aspect ratio for the biwedge cross section. The solution becomes symmetric by an aspect ratio of 0.6.

Figure 12 shows the computed crossflow streamline patterns for a selection of aspect ratios for all three cross sections. Four vortices are present in the streamline patterns for the elliptic and biparabolic sections. The biwedge cross section shows a different behavior. At an aspect ratio of 1, six vortices clearly exist in the asymmetric flow pattern. This behavior had not been seen for circular, elliptic, or the parabolic cross section.

Hence, this study shows that the asymmetric solutions are certainly not unique to circular cones and that the type of cross section seems to play less of a role in determining whether asymmetric behavior occurs in comparison to the effects of Mach number, major axis half-angle, and ratio of major to minor axis or thickness ratio. The study indicates that steady asymmetric behavior does rapidly diminish as the aspect ratio becomes less than unity, and that steady asymmetric conical

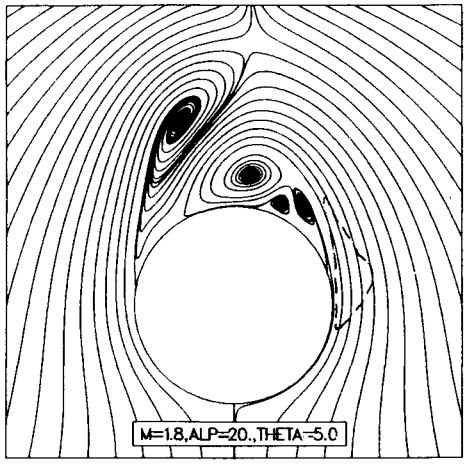

Fig. 10 The effect of a strake on the asymmetry of a 5-deg circular cone at $M_\infty = 1.80$ and $\alpha = 20$ deg.

solutions much below a thickness or aspect ratio of 0.5 do not seem to exist at $\alpha/\theta = 4.0$. This explains why the addition of a thin strake to the nose of an aircraft promotes lateral stability.

Ogive Cylinder Body

A parabolized solution was computed for a 5-deg cone ogive cylinder body at $M_\infty = 1.80$, $\alpha = 20$ deg as shown in Fig. 13. The parabolized solution was started with a local conical asymmetric solution at $R = 1$. The body expanded to a cylinder at $R = 5$ and the computation terminated at $R = 20$. A finer grid of (195 × 96 × 27) was used for the computations. Figure 13b shows the details of the vortex behavior beginning just prior to the cylindrical portion of the body. A vortex street-like behavior with spatial distance develops rapidly on the cylindrical portion of the body. Figure 14 shows the sideforce coefficient per unit length as a function of axial distance. The sideforce exhibits a periodic behavior reflecting the periodic alternating nature of the vortices on the surface of the body.

Conclusion

A study of slender circular cones has demonstrated that a regime of naturally occurring asymmetric locally conical steady solutions exists for 5- to 7-deg cone half-angles for Mach numbers less than 3 and incidence of 20 deg. A study of three different cross-sectional shapes (i.e., elliptic, biparabolic, and

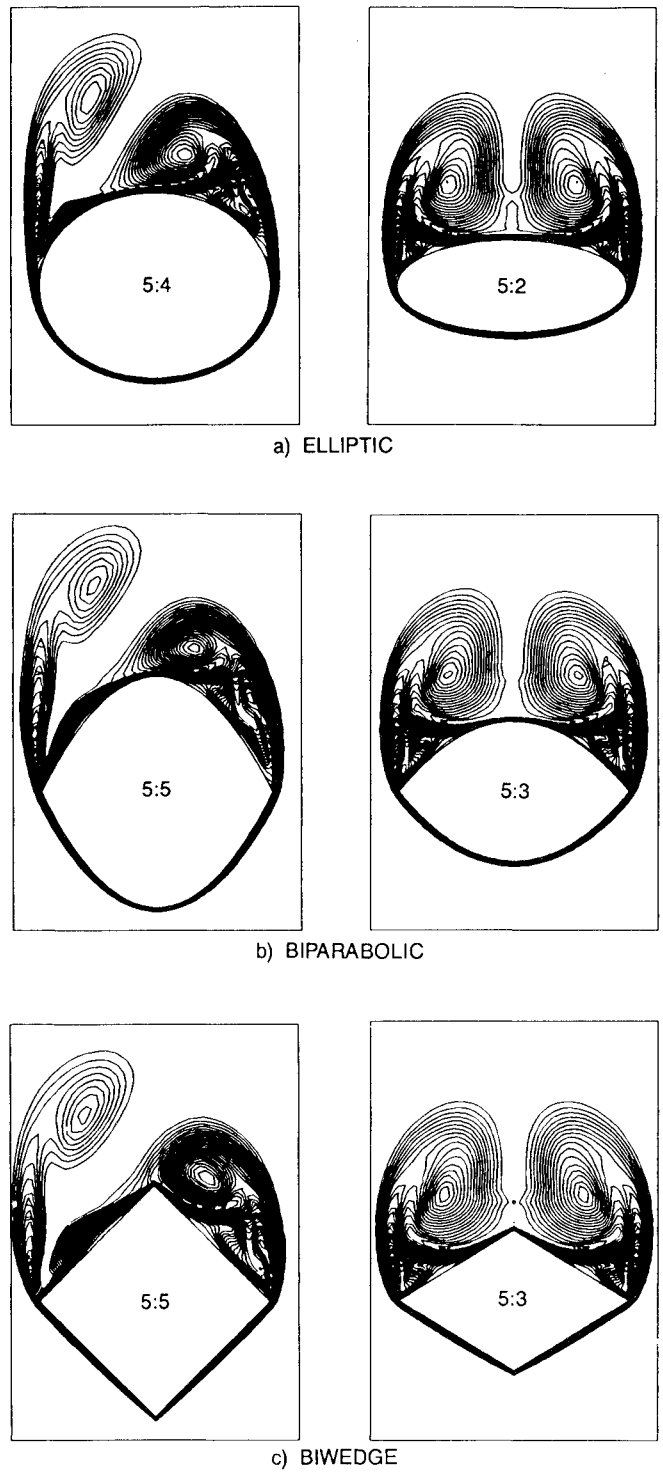

Fig. 11 Entropy contours computed for three different cross sections with 5 deg half-angles and varying aspect ratios at $M_\infty = 1.80$ and $\alpha = 20$ deg.

biwedge) shows that asymmetric conical solutions are certainly not unique to circular cones and exist for other cross-sectional shapes. A study of the effect of aspect ratio or thickness indicates that steady asymmetric conical solutions may not exist for aspect ratios less than 0.4. The elimination of asymmetric flow behavior with the use of strakes was also demonstrated.

A supersonic parabolized Navier-Stokes solution for an ogive cylinder body also demonstrated and verified the global amplification of local asymmetries established at the nose of the body similar to the findings of Refs. 4 and 5. The relationship

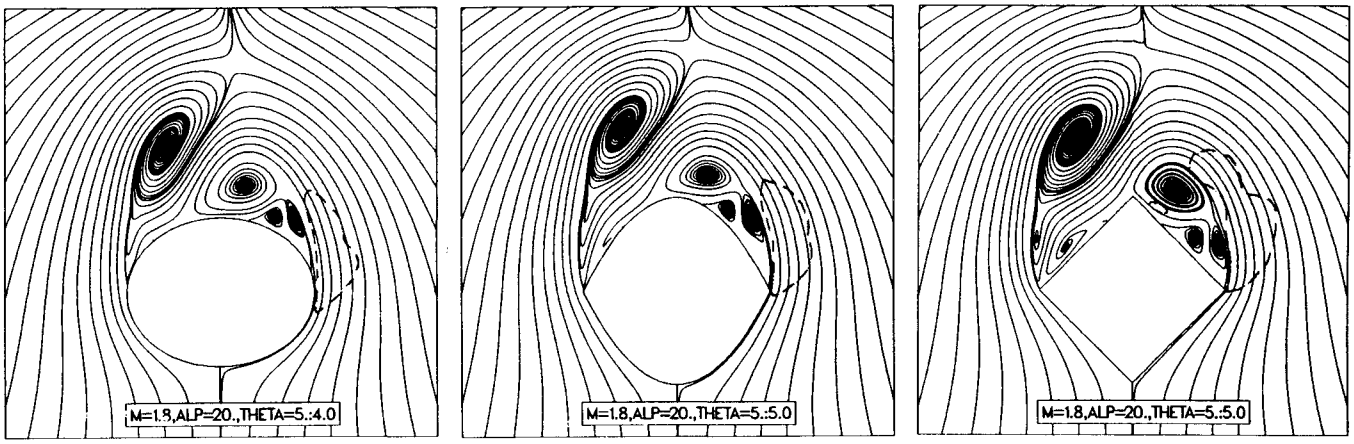

Fig. 12 Crossflow streamline patterns computed for three different cross sections with 5-deg half-angles and varying aspect ratios at $M_\infty = 1.80$ and $\alpha = 20$ deg.

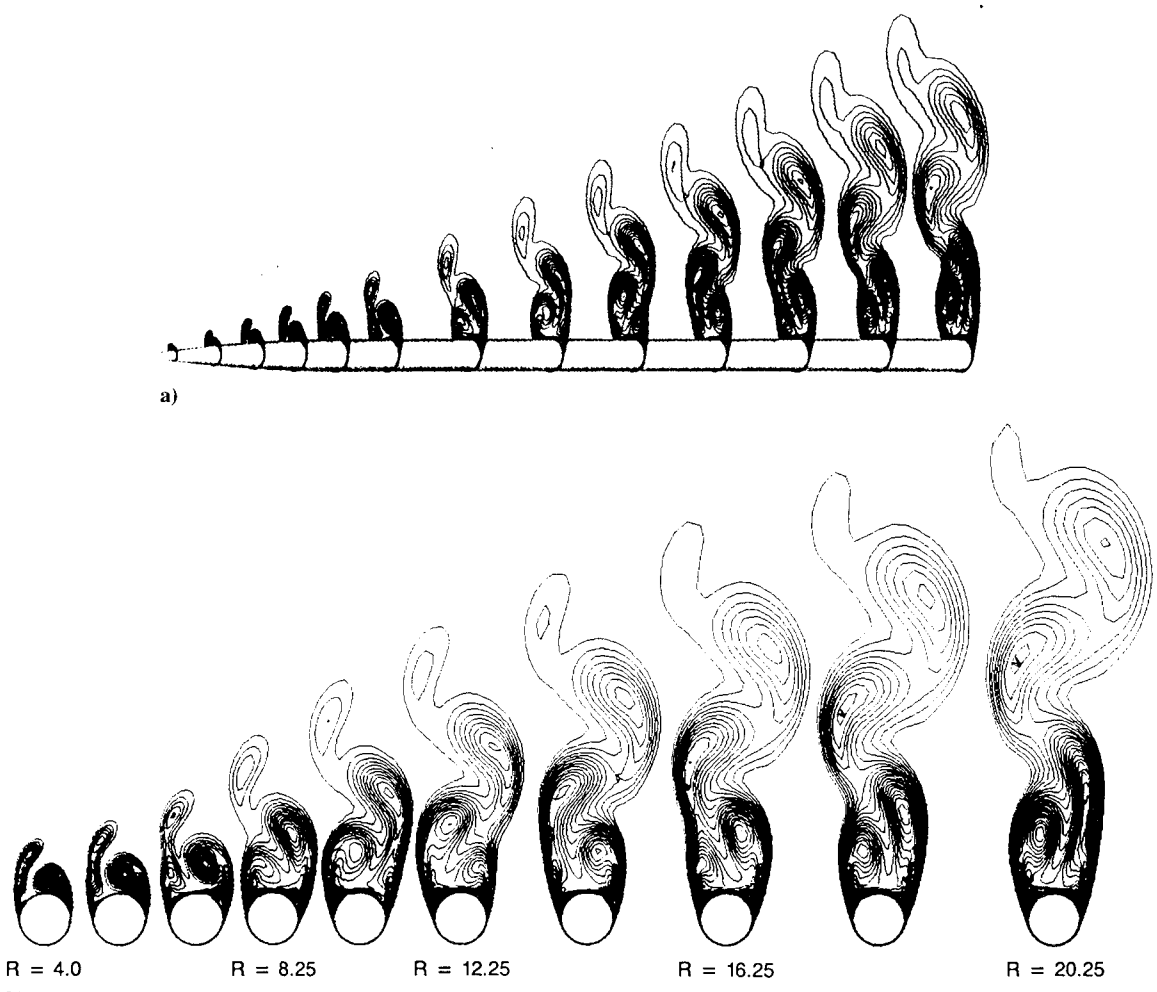

Fig. 13 Selected entropy contours at several radial stations for a 5-deg ogive cylinder body at $M_\infty = 1.80$ and $\alpha = 20$ deg.

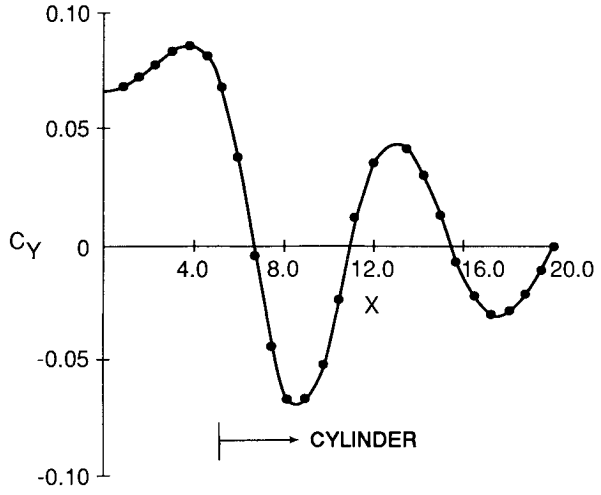

Fig. 14 Sideforce coefficient per unit length as a function of axial distance computed for a 5-deg ogive cylinder body at $M_\infty = 1.80$ and $\alpha = 20$ deg.

of these naturally occurring local conical asymmetric flows to fully three-dimensional flows is still not clear and warrants further study.

References

[1]Fiddes, S. P., "Separated Flow About Cones at Incidence-Theory and Experiment," *Proceedings of Symposium on Studies of Vortex Dominated Flow*, NASA/LRC, 1985.

[2]Marconi, F., "Asymmetric Separated Flows about Sharp Cones in a Supersonic Stream," *Proceedings of the 11th International Conference on Numerical Methods in Fluid Dynamics*, Williamsburg, VA, 1988.

[3]Siclari, M. J., and Marconi, F., "The Computation of Navier-Stokes Solutions Exhibiting Asymmetric Vortices," AIAA 20th Fluid Dynamics, Plasma Dynamics and Lasers Conference, AIAA Paper 89-1817, Buffalo, NY, June 1989.

[4]Degani, D., and Schiff, L. B., "Numerical Simulation of the Effect of Spatial Disturbances on Vortex Asymmetry," AIAA 27th Aerospace Sciences Meeting, AIAA Paper 89-0340, Reno, NV, Jan. 1989.

[5]Degani, D., "Numerical Investigation of the Origin of Vortex Asymmetry," AIAA 28th Aerospace Sciences Meeting, AIAA Paper 90-0593, Reno, NV, January 1990.

[6]Kandil, O. A., Wong, T. C., and Liu, C. H., "Prediction of Steady and Unsteady Asymmetric Flows Around Cones," AIAA 28th Aerospace Sciences Meeting, AIAA Paper 90-0598, Reno, NV, Jan. 1990.

[7]Thomas, J. L., Van Leer, B., and Walters, R. W., "Implicit Flux-Split Schemes for the Euler Equations," AIAA 18th Fluid Dynamics and Plasmadynamics and Lasers Conference, AIAA Paper 85-1680, Cincinnati, OH, July 1985.

[8]Siclari, M. J., DelGuidice, P., and Jameson, A., "A Multigrid Finite Volume Method for Solving the Euler and Navier-Stokes Equations for High Speed Flows," AIAA 27th Aerospace Sciences Meeting, AIAA Paper 89-0283, Reno, NV, Jan. 1989.

[9]Siclari, M. J., and DelGuidice, P., "A Hybrid Finite Volume Approach to Euler Solutions for Supersonic Flows," AIAA 26th Aerospace Sciences Meeting, AIAA Paper 88-0225, Reno, NV, Jan. 1988.

[10]Jameson, A., "A Vertex Based Multigrid Algorithm for Three-Dimensional Compressible Flow Calculations," ASME Symp. on Numerical Methods for Compressible Flow, Anaheim, CA, Dec. 1986.

[11]Fiddes, S. P., "A Theory of the Separated Flow Past a Slender Elliptic Cone at Incidence," AGARD CP 291, Paper 30, 1980.

[12]Peake, D. J., and Owen, F. K., "Control of Forebody Three-Dimensional Flow Separation," AGARD-CP-262, 1979, pp. 15-1 to 15-46.